

On the occurrence of Balmer spectra in expanding liquid hydrogen microplasmas

C. Fortmann, T. Döppner, A. Przystawik, T. Raitza, G. Röpke, J. Tiggesbäumker, N.X. Truong
Universität Rostock, Institut für Physik, 18051 Rostock, Germany

T. Laarmann
Max-Born-Institut, Max Born Strasse 2a, 12489 Berlin, Germany
 (Dated: May 26, 2019)

Balmer spectra are investigated which are obtained from liquid hydrogen targets irradiated by ultra-short intense laser pulses. Starting from a general quantum statistical approach, a unified description of bremsstrahlung, the Stark broadening and the van der Waals profile of hydrogen spectral lines is used, which allows for the inclusion of many-particle effects. Analyzing the line profiles, a low ionization degree of a dense plasma is inferred, where the main contribution to the spectral line shape originates from the interaction with the neutral components. A consistent description of the Balmer spectra can be given within plasma hydrodynamics describing the formation of excited atomic states in the expanding microplasma only below a critical density. The time-integrated measured spectra can be analysed to deduce signatures for the time-dependent temperature and density. Reasonable agreement of observed spectra with the time evolution of the microplasma parameters in a hydrodynamical calculation is found.

Keywords: Spectral line profiles, laser excited clusters, van der Waals broadening, expanding hydrogen microplasmas

PACS numbers: 51.70.+f, 52.50.Os, 52.50.Jm, 32.70.Jz, 36.40.Vz

I. INTRODUCTION

Spectroscopy is one of the most powerful methods in plasma diagnostics. In particular, the analysis of the shape of spectral lines allows to determine the properties of the plasma such as temperature, density and composition. For dense, strongly coupled plasmas, optical spectra have been investigated to infer the parameter values not only of laboratory, but also of astrophysical plasmas, see, e.g., Refs. [1, 2, 3, 4] and Refs. [5, 6, 7], respectively.

The shape of spectral lines is determined by different processes. Besides the natural line width given by the finite lifetime of excited states, Doppler broadening is related to the thermal motion of the emitters. The influence of the surrounding medium becomes more important at increasing density and leads to pressure broadening. A large effect is caused by charged particles in the plasma. This Stark broadening is determined by the distribution of ions as sources of the microfield, whereas the contribution of the electrons usually is treated in *impact approximation* [8, 9]. The Weisskopf radius can be used to distinguish between collision parameters where the collision is strong or weak. However, also the neutral components in the surrounding medium contribute to the shape of spectral lines what is denoted as van der Waals broadening. In general, the shape of spectral lines is characterized not only by the width, but also the shift and asymmetry so that the full line profile has to be investigated [10].

A systematic approach to the shape of spectral lines in dense plasmas has been worked out on the basis of perturbation theory, and many-particle effects have been incorporated. Griem [11] gives a review of different classical and semiclassical methods as well as the application to different plasma line shapes. A quantum statistical approach based on the many-particle Green functions method was presented by Günter [12, 13] and has been worked out systematically for charged perturbers. Special attention was paid to show the equivalence between this rigorous approach and the aforementioned classical and semiclassical approaches in the appropriate limits. The quantum statistical approach has been applied to a broad range of systems, e.g. hydrogen plasmas [12, 14, 15, 16], helium plasmas [17, 18] and plasmas of other elements containing H or He like ions. In most cases, the situation of a hot and dense plasma with a large fraction of free electrons was considered. In such systems, the main contributions to the shift and width of a given spectral line, besides the natural line width and Doppler broadening, come from the ionic microfield, caused by ions surrounding the radiating atom or ion, collisions with free electrons, and interaction with collective excitations in the plasma (plasmons). Theoretical results are in very good agreement with experiments, e.g. by Wilhein [19, 20].

The influence of neutral perturbers becomes dominant if the ionization degree of the partially ionized plasma is low. Van der Waals broadening has been investigated within second order perturbation theory. Based on the derivation of the van der Waals potential between two hydrogen atoms in their ground state as given by London [21], a red shift of the spectral line follows as was shown by Margenau [22]. A review of van der Waals broadening is given by Traving [23].

We show how to extend the quantum statistical approach, elaborated for the influence of charged particles on the line profile, to include also the interaction with neutral perturbers. In this way, the extension of the van der Waals

broadening by accounting for many-particle effects such as dynamical screening or strong collisions is possible. A unified description of the influence of the perturbing partially ionized plasma on the line profile of a radiating atom can be performed, treating charged particles and neutrals within the same formalism.

The theory will be applied to the investigation of optical spectra obtained from hydrogen microdroplets heated by strong femtosecond laser pulses. So far, most of the experimental and theoretical work has concentrated on nanosized clusters [24, 25, 26]. Studies on the light emission from these systems have focused on x-rays and EUV-radiation [27, 28, 29], motivated by the search for novel light sources. Hydrogen as a target material has attracted considerable attention since nuclear fusion has been demonstrated as a result of Coulomb exploding deuterium clusters [30]. Various efforts to produce micrometer sized hydrogen targets are reported, cf. e.g. Ref. [31]. Other studies on such large systems include, e.g., the measurement of x-ray emission from Kr clusters [32] and from methanol microdroplets [33]. An expanding microplasma can be produced with interesting parameter values. In particular, strongly coupled plasmas are obtained, but with temperature and density changing in time. Thus, a nonequilibrium description is necessary to follow the time evolution of the excited microplasma. On the other hand, time resolved experimental techniques have been demonstrated to measure transient plasma properties like the evolution of the plasma density [34, 35].

In the experiment on μm sized droplets reported here, lines of the hydrogen Balmer series are observed as distinctive features in the optical emission spectrum. The present paper will give a first interpretation of the recorded line shapes. In particular we will show that a dynamical picture is necessary to describe the observed spectra, and we are able to get information about the stages relevant for the line emission. Since the line profiles show a strong influence of neutral perturbers, the van der Waals broadening is of special interest.

The work is organized as follows: In the second section we will briefly outline the method of thermodynamic Green functions with emphasis on its application to the field of spectral line shapes. The method will be applied to the case of a weakly ionized plasma, where the interaction among atoms is governed by the dipole-dipole term. The Margenau result appears in the case of ground state perturbers. In the third section, our results will be compared to Balmer spectra obtained from laser produced hydrogen microplasmas. The characteristic asymmetric red shift observed in these experiments can be explained in terms of a van der Waals profile. Parameter values for an effective temperature and density are inferred. However, an equilibrium picture cannot give a consistent description of the measured Balmer spectra, and a dynamical picture of the expanding microplasma is demanded. In the fourth section, a hydrodynamical description of the expanding droplet after laser excitation is given, which allows to interpret the observed spectra if considering the time stages where excited atomic states can exist.

II. MANY-BODY THEORY OF LINE SHAPES AND VAN DER WAALS BROADENING

A. Quantum statistical approach to spectral line shapes

A quantum statistical approach to the optical spectra of dense, strongly coupled systems can be given within linear response theory. Emission and absorption of radiation is related to the transverse dielectric function $\epsilon_{\text{tr}}(\vec{k}, \omega)$. In the optical region, the wavelength is large compared with atomic distances so that the long-wavelength limit $k \rightarrow 0$ can be considered. For the absorption coefficient we find

$$\alpha(\omega) = \frac{\omega}{cn(\omega)} \text{Im} \epsilon(0, \omega) , \quad (1)$$

$n(\omega)$ is the refraction index, c is the velocity of light in vacuum. For $k \rightarrow 0$ the transverse and longitudinal dielectric function $\epsilon(0, \omega)$ become identical. We consider in the following the longitudinal one.

The dielectric function for a charged particle system can be evaluated in a rigorous way using quantum statistical methods. According to $\epsilon(\vec{k}, \omega) = 1 - (1/\epsilon_0 k^2) \Pi(\vec{k}, \omega)$, it is linked to the polarization function $\Pi(\vec{k}, \omega)$, for which a systematic perturbation expansion can be given. A Green function approach to the polarization function is outlined in App. A. Using Feynman diagrams and partial summations, appropriate approximations can be found which account for different microscopic processes contributing to the behavior of the charged particle system. In particular, for partially ionized plasmas a cluster decomposition $\Pi(\vec{k}, \omega) = \Pi_1(\vec{k}, \omega) + \Pi_2(\vec{k}, \omega) + \dots$ can be performed to give the contribution of free carriers as well as of bound states in a systematic way [36].

$\Pi_1(\vec{k}, \omega)$ collects the single-particle contribution. In lowest order, neglecting collisions with other particles, the well-known RPA polarization function

$$\Pi_1^{(0)}(\vec{k}, \omega) = \Pi^{\text{RPA}}(\vec{k}, \omega) = \sum_{c, \vec{p}} e_c^2 \frac{f_c(\vec{p}) - f_c(\vec{p} - \vec{k})}{E_p^c - E_{\vec{p}-\vec{k}}^c - \hbar\omega - i\eta} \quad (2)$$

is obtained. Here, $f_c(\vec{p}) = [\exp\{(E_p^c - \mu_c)/k_B T\} + 1]^{-1}$ is the Fermi distribution function of particles of species c (including spin) with charge e_c and mass m_c , $E_p^c = \hbar^2 p^2/2m_c$ is the single-particle kinetic energy, and μ_c the chemical potential. Within this lowest order approximation, single-particle excitations as well as collective plasmon modes are described. The limit $\eta \rightarrow 0^+$ has to be performed after the summation over momenta.

The RPA contribution $\Pi_1^{(0)}(\vec{k}, \omega)$ is improved if interactions with other particles beyond mean field are included, see App. A. Medium effects, such as collisions, dynamical screening and exchange, enter the polarization function via the single-particle self-energies and the vertex function. The vertex function describes the in-medium coupling of particles to the radiation field. It has to be taken in the same approximation as the self-energy as dictated by consistency constraints, i.e. Ward identities [37]. Going beyond the mean-field (Hartree-Fock) approximation, collisions can be considered in lowest order Born approximation. Higher orders lead to dynamical screening and t matrix expressions for strong collisions. This way, the continuum of optical spectra is described, in particular inverse bremsstrahlung [38]. However, line spectra are missing in $\Pi_1(\vec{k}, \omega)$.

The next term in the cluster decomposition is $\Pi_2(\vec{k}, \omega)$. It is given by the convolution of two atomic (two-particle) propagators and describes also transitions between bound states, i.e. the line spectrum [36]. In the lowest order any interaction with further particles are neglected. Similar to $\Pi_1^{(0)}(\vec{k}, \omega)$ given above, replacing single-particle propagators by atomic propagators one obtains

$$\Pi_2^{(0)}(\vec{k}, \omega) = 4 \sum_{\alpha_1 \alpha_2, \vec{P}} \left| M_{\alpha_1 \alpha_2}^{(0)}(\vec{k}) \right|^2 \frac{g(E_{\alpha_1 \vec{P}}^{(0)}) - g(E_{\alpha_2 \vec{P} - \vec{k}}^{(0)})}{E_{\alpha_1 \vec{P}}^{(0)} - E_{\alpha_2 \vec{P} - \vec{k}}^{(0)} - \hbar\omega - i\eta}. \quad (3)$$

The factor 4 accounts for spin degeneration, $g(E_{\alpha \vec{P}}^{(0)}) = [\exp\{(E_{\alpha \vec{P}}^{(0)} - \mu_i - \mu_e)/k_B T\} - 1]^{-1}$ is the Bose distribution function of electron-ion bound states at $E_{\alpha \vec{P}}^{(0)} = -Z^2 \text{Ry}/n^2 + \hbar^2 P^2/2M$, with $\alpha = \{n, l, m, m_s\}$ denoting the internal quantum numbers, $\hbar \vec{P}$ the center of mass momentum, and $M = m_i + m_e$. The unperturbed matrix elements $M_{\alpha_1 \alpha_2}^{(0)}(\vec{k})$ are given by

$$M_{\alpha_1 \alpha_2}^{(0)}(\vec{k}) = e \sum_p \psi_{\alpha_1}^*(\vec{p}) \left[\psi_{\alpha_2}(\vec{p} - \frac{m_e}{M} \vec{k}) - \psi_{\alpha_2}(\vec{p} + \frac{m_i}{M} \vec{k}) \right] \quad (4)$$

$$\simeq e \left[\delta_{\alpha_1 \alpha_2} - \int d^3 \vec{r} \psi_{\alpha_1}^*(\vec{r}) e^{i\vec{k} \cdot \vec{r}} \psi_{\alpha_2}(\vec{r}) \right]. \quad (5)$$

$\psi_\alpha(\vec{p}) = \langle \vec{p} | \alpha \rangle$ and $\psi_\alpha(\vec{r}) = \langle \vec{r} | \alpha \rangle$ are atomic wave-functions in relative momentum representation and coordinate representation, respectively. Eq. (5) results for $m_e/m_i \rightarrow 0$. In contrast to a simple chemical picture where a mixture of free charge carriers and atoms is considered, scattering states are included, and double counting of diagrams has to be avoided. In this approximation, one obtains the unperturbed line-spectrum of isolated atoms including the Doppler profile due to thermal motion.

As before, medium effects are described by taking the self-energy of the constituents and the vertex into account, which now are given on the two-particle level, see App. A. In the simplest approximation, the dynamically screened interaction can be considered similar to the *GW* approximation for the single-particle propagator [39]. This dynamically screened interaction contains the polarization function, which once more can be decomposed into the contribution of single-particle states, two-particle states and higher cluster states. This way we obtain the dynamically screened Born approximation for collisions with free particles or composed clusters of the partially ionized plasma. Before discussing these contributions more in detail, we mention that the Born approximation can be improved for strong collisions considering further terms leading to the t matrix.

In the case of dense and strongly ionized systems, the main contribution to the self-energy comes from the interaction of the radiating atom with charged particles, i.e. electrons and ions. The influence of free particles is given by the RPA-polarization function, i.e. the first term in the cluster decomposition. This interaction can be inserted into the self-energy, but the vertex-function has to be taken in the same approximation. Reducing the screened interaction to its one-loop approximation, which amounts to the second Born approximation with respect to the *statically screened* Coulomb potential, the so-called *impact-approximation* is obtained. Systematic improvements by taking higher order contributions into account lead to the dynamical screening of the Coulomb potential in the case of weak collisions and the t-matrix approach in the case of strong collisions. In particular, the contribution of collisions with electrons to the line profile in dense plasmas is treated this way, for a review see Günter [13].

The following expression for the line-profile $\mathcal{L}(\Delta\omega)$ as a function of the frequency displacement $\Delta\omega = \omega - (E_i^0 - E_f^0)/\hbar$

is obtained [13],

$$\begin{aligned} \mathcal{L}(\Delta\omega) = & \sum_{ii'ff'} M_{if}^{(0)}(\vec{k}) \left[M_{i'f'}^{(0)}(\vec{k}) \right]^* \frac{e^{-\beta\hbar(\omega_{if}+\Delta\omega)} (\omega_{if} + \Delta\omega)^4}{8\pi^3 c^3} \int \frac{d^3P}{(2\pi)^3} e^{-\beta\frac{\hbar^2 P^2}{2M}} \int_0^\infty d\bar{\beta} W_\rho(\bar{\beta}) \\ & \times \langle i | \langle f | \left[\hbar\Delta\omega - \frac{\hbar^2 \vec{P} \cdot \vec{k}}{M} - \frac{\hbar^2 k^2}{2M} - \text{Re} \{ \Sigma_i(\Delta\omega, \bar{\beta}) - \Sigma_f \} + i\text{Im} \{ \Sigma_i(\Delta\omega, \bar{\beta}) + \Sigma_f \} + i\Gamma^v \right]^{-1} | f' \rangle | i' \rangle. \end{aligned} \quad (6)$$

Here, Σ_i, Σ_f denote the electronic contribution to the self-energy of the initial or final state, respectively, Γ^v the vertex contribution. The impact approximation, improving the Born approximation by accounting for dynamical screening and strong collisions, has extensively been discussed in the literature [11].

Due to their large masses, ions are much slower than electrons. In the adiabatic limit, the ions may be considered as a static distribution of charged particles during the process of emission. Considering different ionic configurations in the plasma, the distribution $W_\rho(\bar{\beta})$ of the so-called *microfield* $\bar{\beta} = E/E_{\text{Holtmark}}$, $E_{\text{Holtmark}} = (4n_{\text{ion}}/15)^{2/3} Ze/(2\epsilon_0)$, (n_{ion} is the density of ions in the system) is introduced, and the averaging leads to the Stark profile as given in Eq. (6). Also in the case of ionic contributions, the systematic many-particle treatment leads to further improvements such as the dynamic microfield. We will not detail further the treatment of the influence of free particles on the line shape any further in this paper, we only would give the general many-particle frame because the interaction with bound states can be followed along the same lines.

In the next step, one has to take into account the interaction between the radiator and neutral particles (atoms), as well. This is achieved if the bound state contribution is considered in the cluster decomposition of the polarization function expanding the dynamically screened interaction, see App. A. In particular we will consider the two-particle self-energy describing the influence of the medium on the radiator, where the bound state component is taken into account in lowest approximation. We consider the second order Born approximation with respect to the unscreened Coulomb potential to describe the interaction between neutrals. The detailed calculation is given in the next section.

Again, improvements can be obtained systematically. By calculating the dynamically screened interaction with the polarization function up to the second term in the cluster decomposition, the interaction with free and bound particles as well as with collective excitations could be included in a consistent way. Strong collisions can be described via the four-particle t matrix. In addition to the self-energy term, also the vertex is modified if bound states are included.

B. Evaluation of atom-atom interaction in Born approximation

The calculation of the interaction $V_{\alpha_1\alpha_2}(R)$ between two atoms at distance R in state $|\alpha_1\rangle$ and $|\alpha_2\rangle$, is carried out in App. B. We obtain

$$\begin{aligned} V_{\alpha_1\alpha_2}(R) = & \frac{e^4}{(4\pi\epsilon_0)^2} \sum_{\alpha_3\alpha_4} \frac{1}{E_{\alpha_1}^{(0)} + E_{\alpha_2}^{(0)} - E_{\alpha_3}^{(0)} - E_{\alpha_4}^{(0)}} \\ & \times \left| \sum_{\vec{r}_1\vec{r}_2} \psi_{\alpha_1}^*(\vec{r}_1) \psi_{\alpha_3}(\vec{r}_1) \left[\frac{1}{R} - \frac{1}{|\vec{R} - \vec{r}_1|} - \frac{1}{|\vec{R} + \vec{r}_2|} + \frac{1}{|\vec{R} - \vec{r}_1 + \vec{r}_2|} \right] \psi_{\alpha_2}^*(\vec{r}_2) \psi_{\alpha_4}(\vec{r}_2) \right|^2. \end{aligned} \quad (7)$$

Here, α_3, α_4 denote quantum numbers of the intermediate states. Only elastic processes are considered where the internal quantum numbers for the initial state and the final state are identical. Due to the ion's heavy mass, we neglect the contribution of kinetic energy in the intermediate propagator in comparison with the excitation energies. Besides R which is the distance between the nuclei of the interacting atoms, \vec{r}_1 and \vec{r}_2 are vectors of position of the two electrons of atom 1 and atom 2, respectively.

This result (7) coincides with results from second order perturbation theory. At large distances $R/a_B \ll 1$ we can perform the dipole approximation using $|\vec{R} - \vec{r}|^{-1} \approx 1/R^2 \left[R - (R^2 + r^2 - 2\vec{R} \cdot \vec{r})/2R + 3(R^2 + r^2 - 2\vec{R} \cdot \vec{r})^2/8R^2 \right]$ for $R \gg r$. We obtain the van der Waals potential,

$$\begin{aligned} V_{\alpha_1\alpha_2}^{\text{vdW}}(R) = & \frac{e^4}{(4\pi\epsilon_0)^2 R^6} \sum_{\alpha_1\alpha_2} \frac{1}{E_{\alpha_1}^{(0)} + E_{\alpha_2}^{(0)} - E_{\alpha_3}^{(0)} - E_{\alpha_4}^{(0)}} \\ & \times \left| \sum_{\vec{r}_1\vec{r}_2} \psi_{\alpha_1}^*(\vec{r}_1) \psi_{\alpha_3}(\vec{r}_1) \left[\vec{r}_1 \cdot \vec{r}_2 - 3 \frac{(\vec{r}_1 \cdot \vec{R})(\vec{r}_2 \cdot \vec{R})}{R^2} \right] \psi_{\alpha_2}^*(\vec{r}_2) \psi_{\alpha_4}(\vec{r}_2) \right|^2. \end{aligned} \quad (8)$$

For hydrogen-like atoms the sum in Eq. (8) has been performed by Eissenschitz and London [21]. Their result for the interatomic potential between two hydrogen atoms in ground state ($\alpha_1 = \alpha_2 = 1s$) is given by

$$V_{1s,1s}^{\text{vdW}}(R) = -\frac{C_6}{R^6} . \quad (9)$$

The constant C_6 was calculated as $C_6 = 12.94 \text{ Ry } a_B^6$, where $\text{Ry} = 13.6 \text{ eV}$ is the Rydberg energy and $a_B = 0.52 \text{ nm}$ is the Bohr radius.

For the interaction between a radiator in an excited state $\alpha = n, l$ and a perturber in ground state, $\alpha = 1s$, the following expression for the interaction strength $C_6(\alpha, 1s)$, can be derived, as shown in App. C,

$$C_6(\alpha, 1s) = 4 \frac{n^2}{1 + 1/n^2} [5n^2 + 1 - 3l(l+1)] . \quad (10)$$

Note that there is no exchange contribution in Eq. (7), since the distance R is assumed to be large compared with the Bohr radius. At shorter distances, the higher order terms as well as exchange terms have to be taken into account which will diminish the van der Waals behavior at small distances and possibly, in the case of electrons in the triplet state, result in a repulsion due to the exchange contribution.

We would like to emphasize that our approach is able to include many-particle effects such as screening and strong scattering. The simplest approximation to include many-particle effects is to replace the Coulomb interaction in Eq. (7) by a statically screened one. In a more sophisticated approximation a dynamically screened interaction can be considered. Since we start from the elementary components of the plasma, a unified description of the influence of free charge carriers and neutral components on the line shapes in a partially ionized plasma is possible.

C. Van der Waals profiles

Within a general approach, the contribution of the dense medium to the spectral line shape is given by the self-energy and vertex contribution. In the first order of interaction we have the Hartree-Fock mean field, in second order we obtain the impact approximation where collisions are described in Born approximation.

Within this concept, the van der Waals contribution to the self-energy is

$$\Sigma_{\alpha_1}^{\text{vdW}} = \sum_{\alpha_2, P} g(E_{\alpha_2 \bar{P}}^{(0)}) V_{\alpha_1 \alpha_2}^{\text{vdW}}(q=0) , \quad (11)$$

which in coordinate space reads

$$\Sigma_{\alpha_1}^{\text{vdW}} = \sum_{\alpha_2} n_{\alpha_2} \int d^3 R V_{\alpha_1 \alpha_2}^{\text{vdW}}(R) . \quad (12)$$

Here, n_{α_2} is the density of perturbing atoms in state α_2 . In the following, we consider the perturbing atoms in their ground state $\alpha_2 \equiv 0$ [40] and only the radiator in an excited state $\alpha = nl$, $n > 1$.

As already discussed in connection with the ionic contribution to the spectral line shapes, because of the large masses the motion is slow, and we can apply the microfield concept of strong interaction with a given field distribution. The intensity distribution of a given spectral line, due interaction between the radiator in initial and final states $|i\rangle$ and $|f\rangle$, respectively and the perturber in its ground state $|0\rangle$ is obtained by performing an averaging procedure over the distribution of perturbing atoms,

$$I_{if}(\Delta\omega) = \int d^3 \vec{r}_1 \int d^3 \vec{r}_2 \dots \int d^3 \vec{r}_N P_N(\vec{r}_1, \vec{r}_2, \dots, \vec{r}_N) \delta \left(\sum_{j=1}^N V_{i0}(r_j) - V_{f0}(r_j) - \hbar \Delta\omega \right) . \quad (13)$$

Here, $P_N(\vec{r}_1, \dots, \vec{r}_N)$ is the probability density for having atom 1 in the volume element $d^3 \vec{r}_1$ at \vec{r}_1 , atom 2 in the volume element $d^3 \vec{r}_2$ at \vec{r}_2 , etc. The evaluation of the sum (13) in the case of statistically independent atoms, i.e. $P_N(\vec{r}_1, \dots, \vec{r}_N) = 1/V^N$, is shown in App. D.

The result for the dipole limit of the interaction, Eq. (8) is

$$I_{if}^{\text{vdW}}(\Delta\omega) = \Lambda_{if} [-\Delta\omega]^{-3/2} e^{\pi \Lambda_{if}^2 / \Delta\omega} , \quad (14)$$

with $\Lambda_{if} = (2\pi/3) (C_6(i, 0) - C_6(f, 0))^{1/2} n_{\text{atom}}$. Note that $\Delta\omega$ is to be taken at negative values, i.e. the van der Waals interaction shifts the spectral line to smaller energies (red shift). The maximum of the intensity distribution (14) lies at

$$\Delta\omega_{\text{max}} = - \left(\frac{2\pi}{3} \right)^3 C_6 (n_{\text{atom}} a_B^3)^2 \text{ Ry}/\hbar, \quad (15)$$

with $C_6 = C_6(i, 0) - C_6(f, 0)$ and n_0 the number density of (ground state) hydrogen atoms in the system. The full width of half maximum (FWHM) of the line is found as $\gamma = 2.78 \Delta\omega_{\text{max}}$, see also Refs. [10, 22].

III. EXPERIMENTS WITH LASER IRRADIATED HYDROGEN DROPLETS

A. Experimental setup

We observed emission radiation from hydrogen microplasmas, which are excited by intense femtosecond laser pulses. Hydrogen droplets are produced by expansion of pre-cooled H gas at temperatures between 17 and 22 K through a $20 \mu\text{m}$ orifice into the vacuum chamber with a backing pressure of about 8 bar. At these source conditions, liquid H droplets of up to $10 \mu\text{m}$ in diameter leave the nozzle with a density of $n_{\text{liq}} = 4.2 \cdot 10^{22} \text{ cm}^{-3}$. Roughly 10 mm behind the nozzle the droplets are irradiated by laser pulses generated in a Ti-Sapphire laser system with a wavelength of $\lambda_0 = 810 \text{ nm}$ and a pulse energy of $E_{\text{pulse}} = 2.5 \text{ mJ}$. The beam is focussed to a spot with a beam waist of $40 \mu\text{m}$. The pulse length τ is tuned in the range of $\tau = 50 - 1000 \text{ fs}$, corresponding to laser peak intensities between $7.0 \times 10^{15} \text{ W cm}^{-2}$ and $3.5 \times 10^{14} \text{ W cm}^{-2}$.

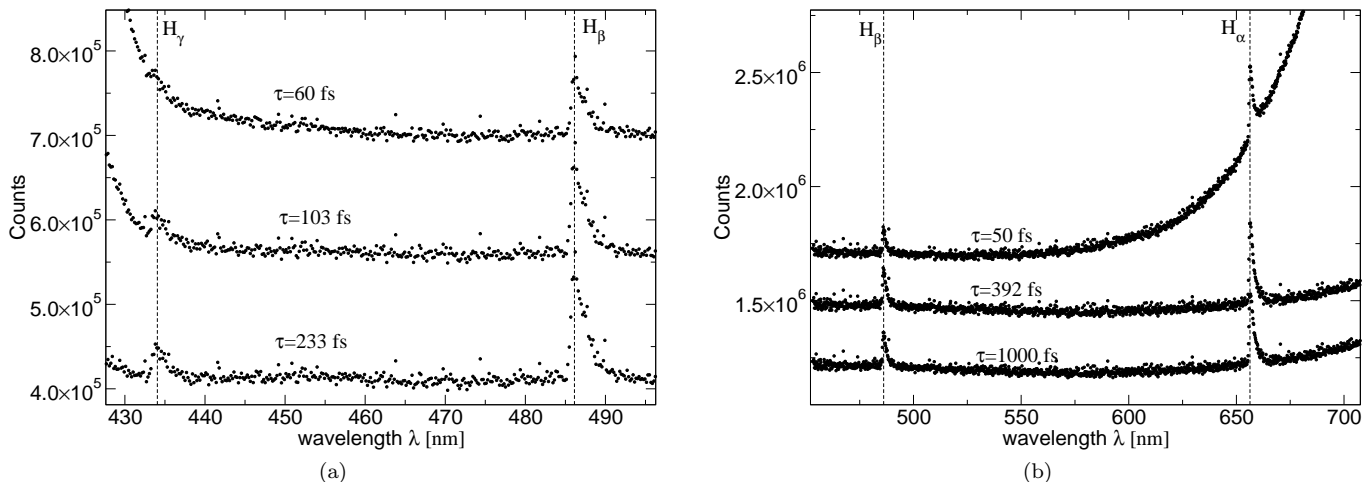


FIG. 1: Representative emission spectra from laser excited H-microplasma in two spectral windows for various pulse lengths. The spectra are shifted by $1.5 \cdot 10^5$ counts (a) and $2.5 \cdot 10^5$ counts (b) with respect to each other. H Balmer spectral lines H_α , 656.3 nm, H_β , 486.1 nm and H_γ , 434.1 nm are given. The large enhancement at long wavelengths ($\lambda > 660 \text{ nm}$) is due to Rayleigh scattering of the laser.

The light emitted by the excited droplets is analyzed by a 0.34 m grating spectrometer (200 lines/mm) and monitored with a CCD camera, providing a spectral dispersion of 0.185 nm per pixel. The entrance slit width was optimized for a high signal, yielding a spectral resolution of $\Delta\lambda \simeq 1 \text{ nm}$. Two regions of the visible spectral range are analyzed in more detail, i.e. (a) $430 \dots 500 \text{ nm}$, and (b) $450 \dots 700 \text{ nm}$. Fig. 1 shows representative emission spectra from the laser excited H microplasmas. Elastic Rayleigh scattering of the incident radiation produces large enhancement of the measured spectra towards the excitation wavelength λ_0 . On top of the background signal, H-Balmer spectral lines are clearly identified, i.e. H_α at $\lambda = 656.3 \text{ nm}$, H_β at $\lambda = 486.1 \text{ nm}$, and H_γ at $\lambda = 434.1 \text{ nm}$.

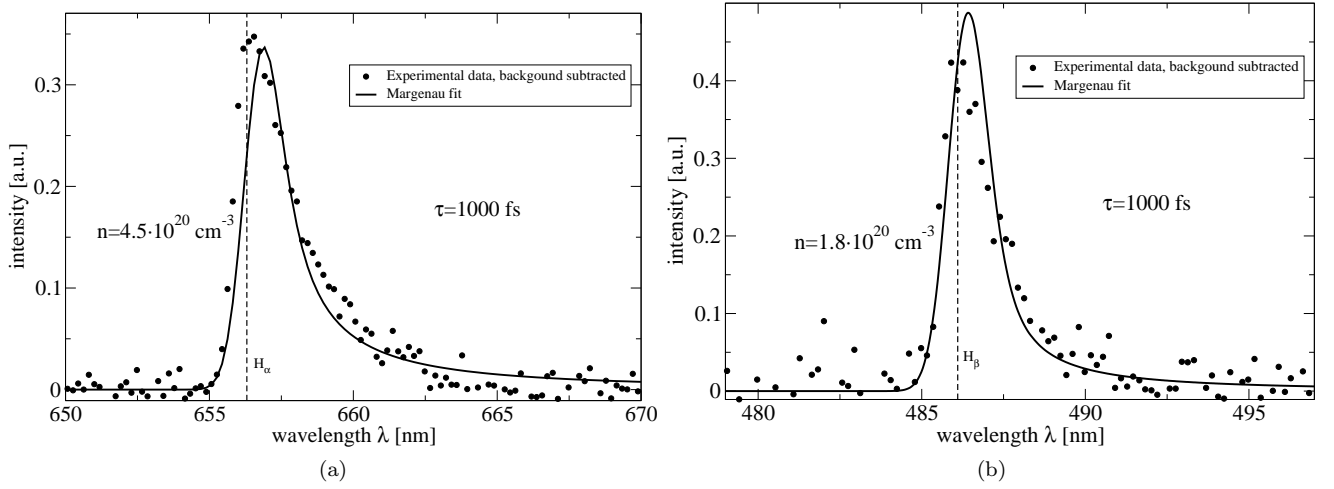


FIG. 2: Comparison of experimental line profiles (solid circles) of H_α and H_β from the $\tau = 1000$ fs data to Margenau theory Eq. (14). For H_α , good agreement between theory and experiment was obtained setting $n_{\text{atom}} = 4.5 \cdot 10^{20} \text{ cm}^{-3}$. For H_β , the best fit was obtained with $n_{\text{atom}} = 1.8 \cdot 10^{20} \text{ cm}^{-3}$.

B. Analysis of the spectra

1. Effective Temperatures

In order to quantitatively analyse the Balmer line signals, we have to subtract the background signal. Therefore, the neighbouring spectral ranges of each line, i.e. 640..655 nm and 670..685 nm for the H_α line, as well as 460..467 nm and 472..480 nm for H_β are fitted by an exponential function, which is then subtracted from the complete data set. As an example, Figs. 2 (a) and (b) show the background subtracted spectra for the case of $\tau = 1000$ fs as solid circles. The solid curves are the Margenau profiles fitted to the data; they will be discussed in more detail in Sec. III B 2.

By comparing integrated intensities from different spectral lines, we can determine the effective temperature in the system. Given the ratio of wavelength-integrated intensities I_1/I_2 of two spectral lines of the same atomic species and the same ionization stage at central wavelengths λ_1 and λ_2 , and assuming again local thermal equilibrium, the effective line temperature is [10]

$$T_{12}^{\text{eff}} = \frac{E_1 - E_2}{k_B \ln \left[\frac{A_1 g_1 \lambda_2 I_2}{A_2 g_2 \lambda_1 I_1} \right]}. \quad (16)$$

A_1 , A_2 are the angular momentum averaged Einstein coefficients for the transition between levels corresponding to the spectral line 1 and 2, respectively and g_1 and g_2 are the degeneracy factors of the excited level (principal quantum number n_i^{ex}) of each transition, i.e. $g_i = 2(n_i^{\text{ex}})^2$. E_1 and E_2 are the energies of the excited level for each transition. Tab. I lists effective temperatures for each pulse length. As can be seen, the effective line temperature is dependent on the pulse length τ of the laser. One obtains different results from the two ratios $I(H_\alpha)/I(H_\beta)$ and $I(H_\beta)/I(H_\gamma)$. For small τ , $T_{\alpha\beta}^{\text{eff}}$ rises with increasing τ . At $\tau \simeq 400$ fs, $T_{\alpha\beta}^{\text{eff}}$ saturates near 1 eV. On the other hand, $T_{\beta\gamma}^{\text{eff}}$ gives values around 0.5 eV.

TABLE I: Effective line temperatures according to Eq. (16) versus pulse length. The first set of figures was obtained from the short wavelength spectrum, shown in Fig. 1(a), the second set comes from the data shown in Fig. 1(b).

τ [fs]	60	103	233	τ [fs]	50	109	170	264	392	695	1000
$T_{\beta\gamma}^{\text{eff}}$ [eV]	0.49	0.56	0.41	$T_{\alpha\beta}^{\text{eff}}$ [eV]	0.57	0.62	0.81	0.97	0.99	1.00	1.04

These effective temperatures have to be analysed within a microscopic description of the expanding source. Self-absorption should be considered so that the intensities occurring in Eq. (16) are modified when propagating through the microplasma. Furthermore, different values T_{12}^{eff} from the intensities of H_α , H_β and H_γ indicates that the system is in a generic non-equilibrium state, which cannot be described by a single temperature. Despite the measured spectra

are time integrated, we have to assume a dynamic evolution of the plasma parameters temperature and density over the course of the expansion of the excited hydrogen droplets. Within a hydrodynamical description given below in Sec. IV B, local thermal equilibrium with plasma parameters depending on space and time are introduced.

During the expansion process, radiation can only be produced if the upper level of the transition in question is existent in the system so that it can be occupied. From simple geometric and energetic arguments it is clear, that $n = 3, 4, 5$ levels are not present in hydrogen at liquid densities. This point will be discussed in more detail in subsection IV C.

The continuum background stems from free-bound and free-free (bremsstrahlung) transitions. The spectral behavior can also be used to estimate effective temperatures which should be analysed within a dynamical expansion model. Since more experimental work is necessary to separate the continuum background radiation, we will consider only the line spectra in this work.

2. Spectral line shapes

To analyze the line profiles, we first have to consider the effect of the broadening due to the finite resolution of the experimental setup. The true line profile is obtained after deconvolution with the detector function. In a separate experiment the spectral resolution was measured as $\Delta\lambda \simeq 1$ nm [41]. This is consistent with the steep increase of intensity on the blue wing of the unperturbed spectral line.

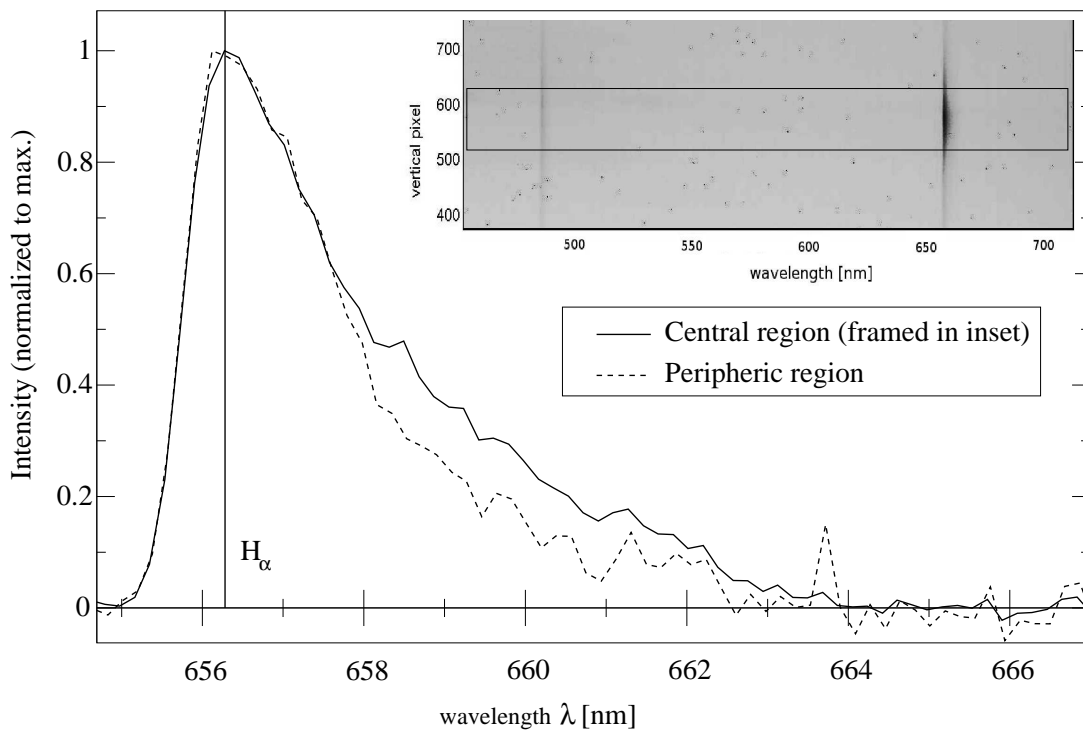


FIG. 3: Normalized spectra near the H_α -line for $\tau = 1000$ fs pulse length. The raw data (c.f. inset) have been summed over different vertical ranges. The solid line marks the central region of the laser focus (framed part in the inset), the dashed curve corresponds to the data from the peripheric region.

On the long wavelength wing, all spectral lines show a significant broadening. In Fig. 3 we analyze the spectral line shape as a function of the distance of the origin of radiation from the plasma's center. This is achieved by integration of the CCD-Data over different ranges in the y -direction, cf. the inset in Fig. 3. We plot the corresponding spectra for the central region of the laser focus (framed part in the inset) and for the peripheric region, about $100 \mu\text{m}$ beside the focus. After background subtraction, the spectra are normalized to their maximum value. In this way it can be seen, that the width of the spectral line depends significantly on the spatial origin of the radiation and decreases with increasing distance from the center. This behaviour indicates that the asymmetric broadening of the spectral lines is related to the properties of the produced microplasma and should be described as a density effect.

Pressure broadening of spectral lines is caused by charged perturbbers as well as by neutral perturbbers. As discussed in Sec. II, free electrons are treated in impact approximation leading to a symmetric Lorentzian line profile, which, however, is smaller than the estimated resolution of about 1 nm. Also the ionic microfield contributes to a Voigt profile with a broadening in the red as well as the blue direction (linear Stark effect) and is also limited by the estimated resolution. Thus we conclude that the influence of free charged particles is not clearly identified so that the free electron density is below $n_e^{\text{free}} = 10^{17} \text{ cm}^{-3}$ which at $T = 1 \text{ eV}$ gives for H_α the FWHM of 1 nm.

The asymmetric red shift can be described by the interaction with neutral perturbbers. We will now compare the experimental data to the line-shape due to interaction with neutral perturbbers, as outlined in Sec.IIB. In Fig. 2, we compare the measured spectra in the vicinity of the H_α line to the emission profile as given by Margenau, Eq. (14), convoluted with the detectors resolution function. In the case of the H_α -line, the best fit was obtained using $n_{\text{atom}} = 4.5 \cdot 10^{20} \text{ cm}^{-3}$ for the density of neutrals. In the case of H_β , the density $n_{\text{atom}} = 1.8 \cdot 10^{20} \text{ cm}^{-3}$ gives the minimum χ^2 .

As already discussed in context with the effective temperatures, the different values of the effective densities contradict an equilibrium picture. Despite the observed line profiles are time integrated, we need a dynamical description of the expanding microplasma to explain the emission of spectral lines during this nonequilibrium process. In the following Section we present a hydrodynamical scenario for the line emission.

IV. MODEL CALCULATIONS AND DISCUSSION

A. Energy deposition

The energy deposition inside the hydrogen droplet can be estimated from the pulse energy of the laser, $E_{\text{pulse}} \simeq 2.5 \text{ mJ} \simeq 1.6 \cdot 10^{16} \text{ eV}$, the ratio of the droplet surface to the focal spotsizes, i.e. $(10 \mu\text{m}/40 \mu\text{m})^2 \simeq 0.06$, and assuming about 50 % absorption inside the droplet, which is initially transparent. We obtain for the deposited internal energy $U \simeq 0.06 \cdot 0.5 \cdot E_{\text{pulse}} = 4.7 \cdot 10^{14} \text{ eV}$. By applying the ideal gas relation $U = 3N_{\text{atom}}k_{\text{B}}T/2$, we can estimate the initial temperature of the droplet, $T_i \simeq 14 \text{ eV}$. Here, $N_{\text{at}} = n_{\text{liq}}V = n_{\text{liq}}\pi d^3/6 = 2.2 \cdot 10^{13}$ is the number of atoms in the droplet. For a more detailed calculation of the initial temperature, the absorption of the laser radiation has to be known more precisely and also the correlation and dissociation energy has to be accounted for. T_i being larger than the effective temperatures inferred from the relative line intensities in Sec. IIIB 1, indicates again, that we have to consider the dynamic evolution of plasma parameters. A convenient method to describe the temporal evolution of the droplet, is hydrodynamic modelling.

B. Hydrodynamic expansion

Hydrodynamic simulations are a versatile tool to infer the dynamics of a strongly coupled many-particle system. In the case of plasmas, hydrocodes have been successfully applied to study these systems under the influence of strong external fields [42] as well as the relaxation of a plasma in an excited state into equilibrium. Here, we will study the hydrodynamic expansion of the excited, i.e. heated H microdroplet after times which are long compared to the pulse length of the laser. Simulations are performed using the hydrocode MULTI2002 [43, 44]. As initial conditions, we assume a homogenous density profile $n(r, t = 0) = n_{\text{liq}} = 4.5 \cdot 10^{22} \text{ cm}^{-3}$ and also homogenous temperature distribution with $T(r, t = 0) = 14 \text{ eV}$. Fig. 4 shows the number density and temperature profiles. The uppermost curve corresponds to $t = 0.01 \text{ ns}$, while the last curve is taken at $t = 1 \text{ ns}$. Both parameters $n(r, t)$ and $T(r, t)$ show a fast decline in the center of the droplet. The density decreases by a factor of 10 every 300 ps. Secondly, all profiles are nearly constant over a long range from the center and decrease quite fast when approaching the rim of the droplet. Therefore, the central values $n(r = 0, t)$ and $T(r = 0, t)$ can be taken as representative values for the whole droplet. The temporal evolution of the central number density and temperature is shown in Fig. 5.

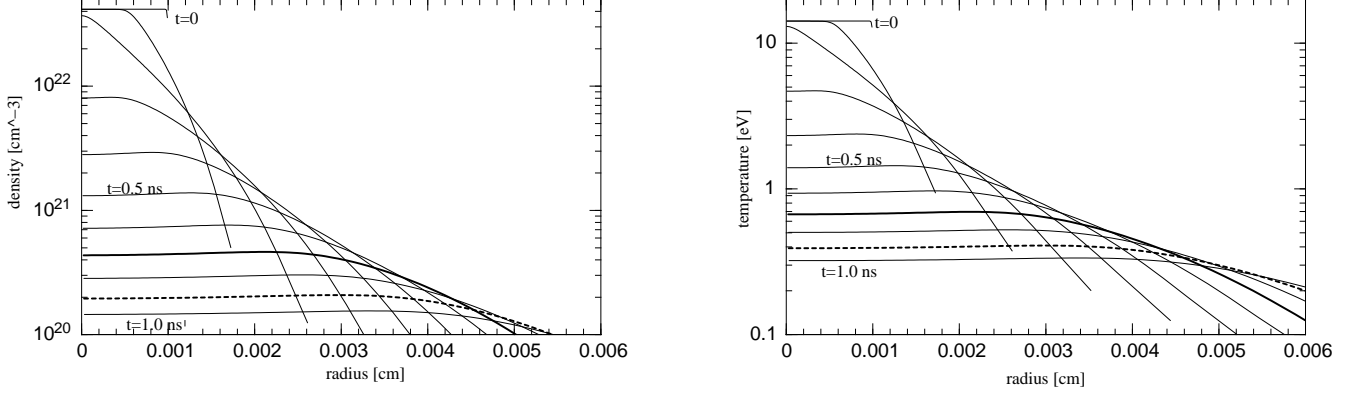


FIG. 4: Hydrodynamic simulation of the density (left) and temperature (right) profiles of expanding liquid hydrogen starting from $n = 4.5 \cdot 10^{22} \text{ cm}^{-3}$ and $T = 14 \text{ eV}$. The broad solid and dashed curves give the conditions after 0.7 ns and 0.9 ns. At this time, the central density has reached the density which has been obtained from the fit of the Margenau profile to the H_α and the H_β spectral line, respectively for $\tau = 1000 \text{ fs}$ pulselength. The corresponding temperatures at these times are close to the effective temperatures $T_{\alpha\beta}^{\text{eff}} \simeq 1 \text{ eV}$ and $T_{\beta\gamma}^{\text{eff}} \simeq 0.5 \text{ eV}$.

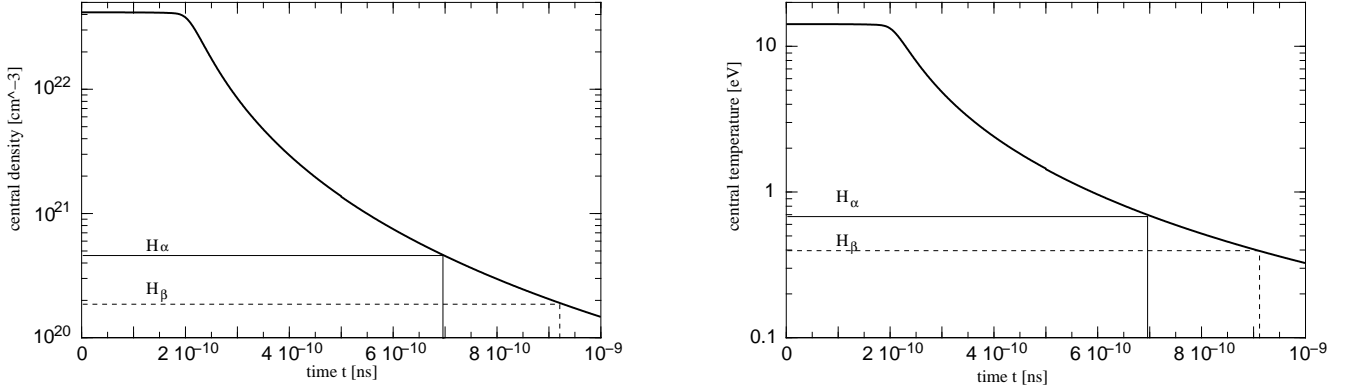


FIG. 5: Temporal evolution of central density $n(r=0,t)$ and temperature $T(r=0,t)$ (fat solid lines). Narrow solid line: central parameters after 0.7 ns, i.e. at the time, when the density obtained in the fit of the Margenau profile to the H_α line, $n = 4.5 \cdot 10^{20} \text{ cm}^{-3}$ is reached. Dashed line: the same for H_β .

The hydrodynamical description gives the time evolution of the excited droplet. The assumption of local thermal equilibrium may be justified on the time scale of ps for the thermalisation of kinetic energies. If we assume also ionisation equilibrium, we can calculate the composition during the time evolution. The temporal behaviour of the ionization is plotted in Fig. 6. For the initial conditions $T = 14 \text{ eV}$ and $n = 4.2 \cdot 10^{22} \text{ cm}^{-3}$, we have an ionization degree $\alpha_e = n_{\text{free}}/n = 0.68$. After $t = 0.7 \text{ ns}$, the density and temperature have decreased so far, that the ionization drops below 10^{-4} . This corresponds to a concentration of free electrons of roughly 10^{17} cm^{-3} . At this density, and $T \simeq 1 \text{ eV}$, the Stark effect leads to a broadening of the H_α line of 1 nm, as was discussed in Sec. IIIB 2. Thus, at times larger than 0.7 ns, Stark broadening does not give a notable contribution to the width of the spectral lines.

C. Occupation of excited levels

In a dense system, the potential energy of an electron in a given atom is modified by the medium. Thus, energy eigenvalues and wave functions are changed due to screening by free charge carriers. In particular, it is well-known that bound states merge with the continuum of scattering states at high densities so that the electrons are no longer

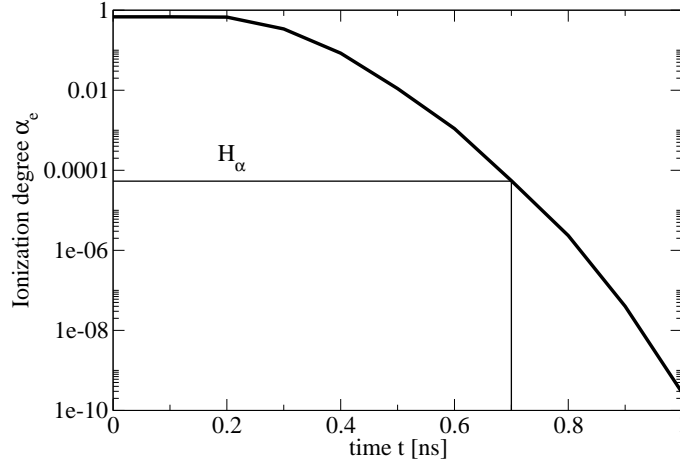


FIG. 6: Ionization degree α_e as a function of time obtained from Saha equation (fat solid curve). The narrow horizontal line gives the ionization after 0.7 ns, i.e. at the time, when the central density has decreased to $4.5 \cdot 10^{20} \text{ cm}^{-3}$, which has been obtained as best-fit parameter in the fit of the Margenau profile to the H_α spectral line.

bound to a special ion, but move relatively free in the plasma as denoted by a transition from dielectric to metallic behavior. Considering excited states, the dissolution occurs already at lower densities so that these excited states cannot longer be occupied to produce a line spectrum.

We focus here to the influence of bound states in the medium to analyse at which densities the excited states are dissolved into the continuum so that no line spectra are formed. In a first approximation, we calculate the modification of the potential in the Schrödinger equation for the hydrogen atom due to the perturbing atoms in the surrounding medium. We consider only ground state atoms and neglect the correlations between the electrons in the perturbing ground state with the radiating electron in the excited state. Solving the Poisson equation, the effective potential is obtained as superposition of the Coulomb potential and the potential of the neighboured atoms, which leads to the lowering of the Coulomb potential.

This lowering of the effective potential has two effects: On the one hand, the energy level is shifted to lower energies, on the other hand, at a certain critical distance, the threshold of potential energy between neighboured atoms crosses the shifted electrons energy level, and the bound state is dissolved into the continuum. This typically happens when the distance between neighbours comes into the range of the extension of the electrons wave-function.

We considered the radiating atom with the electron in the n th energy level, $n = 3, 4, 5$, in the environment of neutral hydrogen atoms in the ground state. At position \vec{R}_i , the contribution to the potential of the latter is obtained solving the Poisson equation,

$$\Delta V_i(\vec{r}) = -\frac{e^2}{4\pi\epsilon_0|\vec{r} - \vec{R}_i|} e^{-2|\vec{r} - \vec{R}_i|/a_B} \left(1 + \frac{|\vec{r} - \vec{R}_i|}{a_B} \right). \quad (17)$$

We assume a closed packed configuration where the radiating atom is surrounded by 12 perturbing next neighbours. The shift of the energy levels with principal quantum numbers $n = 3$ and 4 has been evaluated in first order of perturbation theory and can be given in an analytical form. Results for the shift as a function of the interatomic distance are given in Fig. 7(a).

In Fig 7(b) we give the potential energy $V(r)$ in the direction to a next neighbour for two different distances, together with the corresponding shift of the energy levels with $n = 3$ and $n = 4$. As can be seen, the bound state disappears at a critical distance $R_c^{(n)}$ where the threshold energy becomes lower than the binding energy, and the electron is no longer bound to the central ion, but escapes the effective potential and moves relatively freely within the cluster.

From the critical distance $R_c^{(n)}$, one can then infer the “critical” density $n_c^{(n)}$ that has to be established in the expanding system, before the upper level n of the considered transition can exist, i.e. before the corresponding spectral line can occur. In this way, we obtained for the second excited level, relevant for the H_α transition, a “critical” density of $n_c^{(3)} \simeq 1.24 \cdot 10^{21} \text{ cm}^{-3}$. This value for n_c is by a factor of two larger than the value $n_{\text{atom}} = 4.5 \cdot 10^{20} \text{ cm}^{-3}$ obtained from the fit of the H_α line to the line shape due to van der Waals interaction, cf. Fig. 2(a).

It has to be emphasized in this context, that this are exploratory calculations to estimate the region of density where well-defined excited energy levels of the radiating atom can exist. A more detailed calculation should include electronic

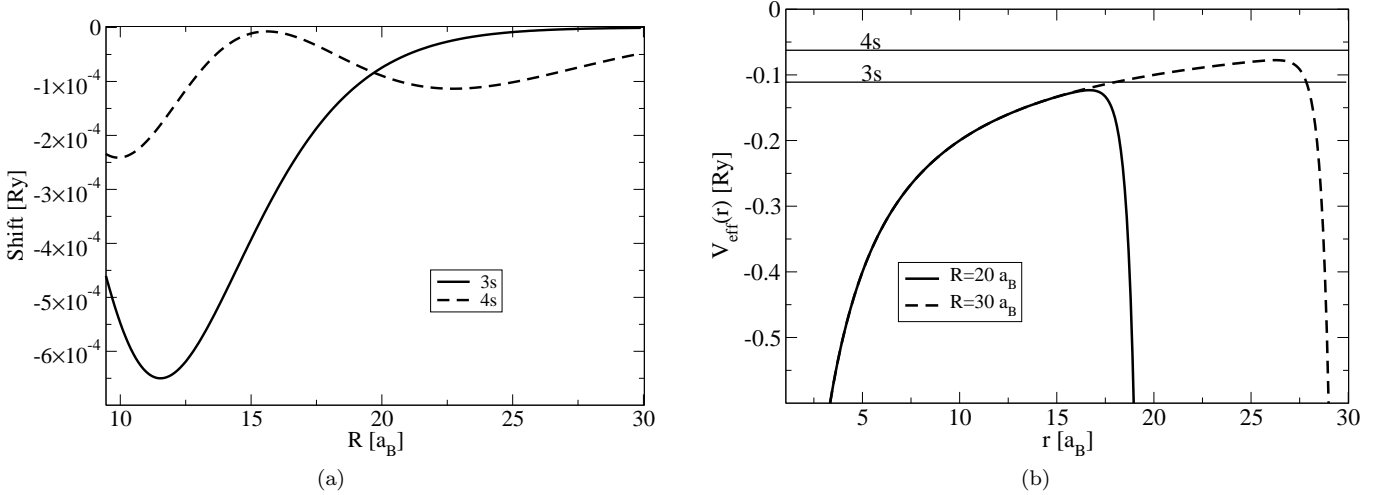


FIG. 7: (a): Energy shift of 3s and 4s levels as a function of the distance R to the next neighbouring atom. (b): Effective potential due to the overlap between the radiator's Coulomb potential and the screened potential of the next neighbouring atom in its ground state. Results are shown for two different values of the interatomic distance $R = 20 a_B$ (blue curve) and $R = 30 a_B$. The perturbed 3s and 4s energies are given as narrow lines.

correlations between radiator and perturber which have been neglected in the calculation of the perturbing potential. The account for correlation and exchange effects will modify the potential and the critical density. In addition, we considered only a perturbing atom at mean distance, neglecting any fluctuations. On the other hand, the spectra are time integrated measurements and hence the density has to be interpreted as a mean value, averaged over the whole exposure time. Initially, i.e. when the radiation begins to take place, the density might in fact be larger than the value inferred from the measured spectra. For H_β , the critical density is obtained as $n_c^{(\beta)} \simeq 2.66 \cdot 10^{20} \text{ cm}^{-3}$, which also exceeds the fit parameter for the H_β line ($n_{\text{atom}} = 1.8 \cdot 10^{20} \text{ cm}^{-3}$) for the same reasons as given above for the case of the H_α line (cf. Fig. 2(b)).

In conclusion, the observed Balmer spectra are not produced in the first stage of the laser excitation of the cluster, because the density of hydrogen in the condensed state is too high to form well-defined excited atomic levels with the corresponding principal quantum numbers. Such levels appear only during the process of expansion and may be used as a signal to infer the state of the microplasma at the corresponding time stage.

D. Line emission scenario

As discussed in the previous Section, the observed Balmer spectra cannot be interpreted within an equilibrium picture of the laser produced microplasma. We could not infer consistent values of plasma parameters for temperature and density. A consistent description is only possible if the time evolution of the expanding microplasma is considered as a non-equilibrium process.

We follow the dynamical expansion of the laser excited hydrogen droplet as given from the hydrodynamical calculation. First we consider the time evolution of the density and determine the time at which the H_α line appears, i.e. where the inferred density $n = 4.5 \cdot 10^{20} \text{ cm}^{-3}$ is reached. Starting with the excitation temperature $T = 14 \text{ eV}$ after the short-pulse laser excitation, this density appears at 0.7 ns. The corresponding temperature obtained from the hydrocode MULTI is $T = 0.65 \text{ eV}$ and is in reasonable agreement with the estimation given in Section 3.2.1. Thus, the H_α line profile reflects the situation of the expanding microplasma after 0.7 ns. In the case of the H_β we observe the following: From the van der Waals fit to the data, cf. Fig. 2(b), $n_{\text{atom}} = 1.8 \cdot 10^{20} \text{ cm}^{-3}$ was obtained, which is reached in the hydrodynamic simulation after $t \simeq 0.9 \text{ ns}$. The temperature is $T \simeq 0.4 \text{ eV}$ at that moment, which is close to the value 0.5 eV obtained from comparing the integrated line intensities of H_β and H_γ , cf. Tab. I. H_β thus gives us information about the state of the droplet at $t \simeq 0.9 \text{ ns}$.

As for the empirically determined plasma parameters, the critical densities for H_α and H_β as discussed in Sec. IV C, have to be compared to the results of the hydrodynamic simulation. The central density of the droplet decreases to the critical density for H_α to appear, $n_c^{(\alpha)} = 1.24 \cdot 10^{21} \text{ cm}^{-3}$ after 0.45 ns. After the same time, the temperature at

the center of the droplet has decreased to 1.3 eV, which is in good agreement with the value 1 eV inferred from the relative line intensities of H_α to H_β .

The critical density for H_β , $n_c^{(\beta)} = 2.66 \cdot 10^{20} \text{ cm}^{-3}$ is reached after 0.8 ns. The central temperature is 0.5 eV at that moment, which coincides again very well with the value 0.5 eV as obtained from the relative line intensities of H_β and H_γ .

This analysis shows, that the droplet in fact undergoes a complex dynamical evolution. The experimental observations can only be understood by modelling the droplets history using hydrocodes. 14 eV as the initial temperature is consistent with the observed temperatures and densities established at later times of the evolution. The line radiation obviously steems from relatively late times in the evolution. What happens before line radiation appears? At the initial conditions of $n_{\text{atom}} = n_{\text{liq}} = 4.2 \cdot 10^{22} \text{ cm}^{-3}$ and $T = 14 \text{ eV}$, the ionization of the droplet can be estimated by 68%, as calculated from solving Saha's equation, cf. Fig. 6. The plasma emission is thus dominated by continuum radiation (free-free and free-bound transitions). However, since the detector integrates over the whole evolution of the plasma, only a flat background remains in the spectrum from this early stage of the evolution. As the ionization goes down, bound states begin to form and line radiation occurs. However, for a given spectral line, both upper and lower level of the corresponding transition have to be well defined. To this end, the density has to go below a certain value, in order to allow for the excited energy level to appear below the effective potential in the dense medium.

Considering the time scales for the expansion of the cluster of the order 10^{-9} s according to the hydrodynamical calculations, the local thermodynamic equilibrium can be assumed, and the life time of the excited states of the order 10^{-11} s is short compared with the evolution of the microplasma. In a more rigorous approach, the variation of temperature and density in space and time should be accounted for to synthesize the spectra.

V. CONCLUSIONS

We found that the investigation of Balmer spectra can be used to get a time-resolved picture of the expanding microplasma produced after irradiating a liquid hydrogen droplet with femtosecond intense laser beams. The line profiles are interesting features of optical spectra which allow for determination of the microplasmas temperature and density over the course of its hydrodynamic expansion. We considered an energy deposition in the liquid hydrogen droplet which is not too high so that in the expanded phase most of the electrons are found in atomic bound states. Thus, the spectral line profiles are determined by van der Waals broadening. We presented a general quantumstatistical approach to line profiles which allows for the unified description of charged and neutral perturbers. In particular, density effects can be included, such as dynamical screening or strong collisions.

Although the spectra are time integrated measurements, we can use the Balmer lines as signatures for the expanding microplasma at definite values of density. To follow the time evolution of an excited droplet more directly, time resolved spectra have to be analyzed. Possibly, this can be achieved with pump-probe experiments and/or stimulated emission measurements.

Acknowledgements

This work has been supported by the Deutsche Forschungsgesellschaft (DFG) through the Collaborative Research Center (SFB) 652. TL acknowledges financial support from the DFG under Grant No. LA 1431/2-1.

-
- [1] R. Flohr and A. Piel, *Phys. Rev. Lett.* **70**, 1108 (1993).
 - [2] L. Godbert, A. Calisti, R. Stamm, B. Talin, S. Glenzer, H.-J. Kunze, J. Nash, R. Lee, and L. Klein, *Phys. Rev. E* **49**, 5889 (1994).
 - [3] M. V. Malyshev and V. M. Donnelly, *Phys. Rev. E* **60**, 6016 (1999).
 - [4] M. Tadokoro, H. Hirata, N. Nakano, Z. L. Petrović, and T. Makabe, *Phys. Rev. E* **57**, R43 (1998).
 - [5] R. Soria, K. Wu, and R. W. Hunstead, *Astrophys. J.* **539**, 445 (2000), astro-ph/9911318.
 - [6] A. O. Benz, *Plasma Astrophysics* (Kluwer Academic Publishers, 2002), 2nd ed.
 - [7] G. B. Rybicki and A. P. Lightman, *Radiative Processes in Astrophysics* (J. Wiley & Sons, New York, 1975).
 - [8] M. Baranger, in *Atomic and Molecular Processes*, edited by D. Bates (Academic Press, New York, 1962), chap. 13.
 - [9] H. Griem and A. Kolb, *Phys. Rev.* **111**, 514 (1958).
 - [10] W. Lochte-Holtgreven, in *Plasma Diagnostics*, edited by W. Lochte-Holtgreven (AIP Press, New York, 1995), chap. 3, p. 135.
 - [11] H. R. Griem, *Plasma Spectroscopy* (McGraw-Hill, New York, 1964).

- [12] S. Günter, L. Hitzschke, and G. Röpke, Phys. Rev. A **44**, 6834 (1991).
- [13] S. Günter, *Optische Eigenschaften Dichter Plasmen* (Rostock, 1995), Habilitation thesis.
- [14] G. Röpke, T. Seifert, and K. Kilimann, Ann. Phys. (Leipzig) **38**, 381 (1981).
- [15] L. Hitzschke, G. Röpke, T. Seifert, and K. Kiliman, J. Phys. B **19**, 2443 (1986).
- [16] A. Könnies and S. Günter, J. Quant. Spectrosc. Radiat. Transfer **52**, 423 (1994).
- [17] V. Milosavljević and S. Djenize, Eur. Phys. J. D **23**, 385 (2003).
- [18] B. Omar, S. Günter, A. Wierling, and G. Röpke, Phys. Rev. D **73**, 056405 (2006).
- [19] T. Wilhein, D. Altenbernd, U. Teubner, E. Förster, R. Häßner, W. Theobald, and R. Sauerbrey, J. Opt. Soc. Am. B **15**, 1235 (1998).
- [20] S. Sorge, A. Wierling, G. Röpke, W. Theobald, R. Sauerbrey, and T. Wilhein, J. Phys. B **33**, 2983 (2000).
- [21] R. Eisenschitz and F. London, Z. f. Physik **60**, 491 (1930).
- [22] H. Margenau, Phys. Rev. **48**, 755 (1935).
- [23] G. Traving, in *Plasma Diagnostics*, edited by W. Lochte-Holtgreven (AIP Press, New York, 1995), chap. 2, p. 66.
- [24] T. Ditmire, T. Donnelly, A. M. Rubenchik, R. W. Falcone, and M. D. Perry, Phys. Rev. A **53**, 3379 (1996).
- [25] T. Döppner, T. Fennel, T. Diederich, J. Tiggesbäumker, and K.-H. Meiwes-Broer, Phys. Rev. Lett. **94**, 013401 (2005).
- [26] K. Kim, I. Alexeev, E. Parra, and H. Milchberg, Phys. Rev. Lett. **90**, 23401 (2003).
- [27] E. Parra, I. Alexeev, J. Fan, K. Kim, S. McNaught, and H. Milchberg, Phys. Rev. E **62**, R7603 (2000).
- [28] M. Schnürer, S. Ter-Avetisyan, H. Stiel, U. Vogt, W. Radloff, M. Kalashnikov, W. Sandner, and P. Nickles, Eur. Phys. J. D **14**, 331 (2001).
- [29] S. Düsterer, H. Schwoerer, W. Ziegler, C. Ziener, and R. Sauerbrey, Appl. Phys. B **73**, 693 (2001).
- [30] K. Madison, P. Patel, M. Allen, D. Price, R. Fitzpatrick, and T. Ditmire, Phys. Rev. A **70**, 053201 (2004).
- [31] O. Nordhage, Z.-K. Lib, C.-J. Fridén, G. Normanc, and U. Wiedner, Nucl. Instr. Meth. Phys. Res. A **546**, 391 (2005).
- [32] S. Hansen, K. Fournier, A. Faenov, A. Magunov, T. Pikuz, I. Skobelev, Y. Fukuda, Y. Akahane, M. Aoyama, N. Inoue, et al., Phys. Rev. E **71**, 016408 (2005).
- [33] M. Anand, P. Gibbon, and M. Krishnamurthy, Opt. Expr. **14**, 5502 (2006).
- [34] J. Zweiback, T. Ditmire, and M. Perry, Opt. Exp. **6**, 236 (2000).
- [35] J. Liu, C. Wang, B. Li, B. Shuai, W. Wang, Y. Cai, H. Li, G. Ni, R. Li, and Z. Xu, Phys. Rev. A **73**, 033201 (2006).
- [36] G. Röpke and R. Der, phys. stat. sol. (b) **92**, 501 (1979).
- [37] G. D. Mahan, *Many-Particle Physics* (Plenum Press, New York and London, 1981), 2nd ed.
- [38] A. Wierling, T. Millat, G. Röpke, R. Redmer, and H. Reinholz, Phys. Plasmas **8**, 3810 (2001).
- [39] C. Fortmann, G. Röpke, and A. Wierling, accepted for publication in Contrib. Plasma Phys., physics/0610262.
- [40] To keep the notation short, we denote the ground state of an atom by $\alpha = 0$. For hydrogen atoms, this has to be read as $nl = 1s$.
- [41] We use the normal distribution $D(\lambda) = \exp(-\lambda^2/2\sigma^2)/\sqrt{2\pi}\sigma$ with $\sigma = 0.425 \cdot \Delta\lambda$, such that $\Delta\lambda$ is the full width at half maximum of the distribution $D(\lambda)$.
- [42] K. Eidmann, J. Meyer-ter Vehn, T. Schlegel, and S. Hüller, Phys. Rev. E **62**, 1202 (2000).
- [43] R. Ramis et al., Comp. Phys. Comm. **49**, 474 (1988).
- [44] R. Ramis et al., Nucl. Fusion **44**, 720 (2004).

APPENDIX A: GREEN FUNCTION APPROACH TO THE POLARIZATION FUNCTION

The general expression for the single state contribution $\Pi_1(\vec{k}, \omega)$ to the polarization function has the form

$$\Pi_1 = \text{Diagram} \quad (A1)$$

The full single-particle propagator contains the self-energy $\Sigma_1(\vec{p}, z)$,

$$\text{Diagram} = \text{Diagram} + \text{Diagram} \quad (A2)$$

The vertex describes the coupling to the electromagnetic field and can also be expressed in terms of an effective interaction kernel. Both quantities have to be approximated in a consistent way. The so-called *GW* approximation

gives the self-energy by the screened potential so that

$$\Sigma^{GW} = \text{diagram: a horizontal line with two arrows pointing right, connected at both ends by a wavy line (photon)}, \quad (\text{A3})$$

whereas the vertex has the form

$$\text{diagram: a vertex with two incoming lines and one outgoing line, labeled } \Gamma = \text{diagram: a vertex with two incoming lines and one outgoing line, labeled } \Gamma^{(0)} + \text{diagram: a vertex with two incoming lines and one outgoing line, labeled } \Gamma^{(0)} \text{ with a wavy line loop on the outgoing line}. \quad (\text{A4})$$

The GW approximation is well studied in condensed matter physics. It describes also the bremsstrahlung and can be further improved accounting for plasma effects.

The two-particle contribution $\Pi_2(\vec{k}, \omega)$ to the polarization function is described accordingly,

$$\Pi_2(\vec{k}, \omega_\mu) = \text{diagram: a loop with two vertices, labeled } M^{(0)} \text{ and } M. \quad (\text{A5})$$

We have the full two-particle propagator

$$G_2(\alpha\vec{P}, \Omega_\lambda) = \text{diagram: a double line with an arrow pointing right} = \frac{1}{\Omega_\lambda - E_{\alpha\vec{P}} - \Sigma_2(\alpha\vec{P}, \Omega_\lambda)}, \quad (\text{A6})$$

with the two-particle self-energy $\Sigma_2(\alpha\vec{P}, \Omega_\lambda)$, and the vertex follows from an equation in analogy to Eq. (A4). Note that one has to take into account that double counting has to be avoided so that scattering states in $\Pi_2(\vec{k}, \omega)$ should not interfere with contributions from $\Pi_1(\vec{k}, \omega)$. Important are the account of bound states in $\Pi_2(\vec{k}, \omega)$.

The higher order corrections to the full vertex $M(\vec{q})$ can be shown to effectively reduce the two-particle self-energy [13] by the amount $i\Gamma^v$. After analytic continuation $\omega_\mu \rightarrow \omega + i0^+$ to real frequencies, we obtain

$$\begin{aligned} \Pi_2(\vec{k}, \omega) = & 4 \sum_{\alpha_1 \alpha_2, \vec{P}} \left| M_{\alpha_1 \alpha_2}^{(0)}(\vec{k}) \right|^2 \left(g(E_{\alpha_1 \vec{P}}^{(0)}) - g(E_{\alpha_2 \vec{P} - \vec{k}}^{(0)}) \right) \\ & \times \left[\omega - E_{\alpha_2 \vec{P} - \vec{k}}^{(0)} + E_{\alpha_1 \vec{P}}^{(0)} - \text{Re} \left\{ \Sigma_{\alpha_2}(E_{\alpha_1 \vec{P}}^{(0)} + \omega) - \Sigma_{\alpha_1}(E_{\alpha_1 \vec{P}}^{(0)}) \right\} + i \text{Im} \left\{ \Sigma_{\alpha_2}(E_{\alpha_1 \vec{P}}^{(0)} + \omega) + \Sigma_{\alpha_1}(E_{\alpha_1 \vec{P}}^{(0)}) \right\} + i\Gamma^v \right]^{-1}. \end{aligned} \quad (\text{A7})$$

Note, that the dependance on ω is neglected in the self-energy of the lower energy level [13].

Neglecting the self-energy and the effective vertex in Eq. (A7), we arrive at Eq. (3).

APPENDIX B: BOUND STATE CONTRIBUTION TO THE TWO-PARTICLE SELF-ENERGY

The interaction between two atoms in state $|\alpha_1\rangle$ and $|\alpha_2\rangle$, moving with momentum \vec{P}_1 and \vec{P}_2 respectively, and carrying Matsubara frequencies Ω_λ and Ω_κ , upon exchange of momentum \vec{k} is given by the following diagram:

$$V_{\alpha_1, \alpha_2}(\vec{P}_1, \vec{P}_2, \Omega_\lambda, \Omega_\kappa, \vec{k}) = \text{Diagram} \quad (\text{B1})$$

$$= \sum_{\alpha_3, \alpha_4} M_{\alpha_1 \alpha_3}^{(0)}(\vec{k}') M_{\alpha_3 \alpha_1}^{(0)}(\vec{k} - \vec{k}') M_{\alpha_2 \alpha_4}^{(0)}(-\vec{k}') M_{\alpha_4 \alpha_2}^{(0)}(\vec{k} + \vec{k}') V_{\vec{k}'} V_{\vec{k} - \vec{k}'} \left[\Omega_\lambda + \Omega_\kappa - E_{\alpha_3 \vec{P}_1 + \vec{k}'}^{(0)} - E_{\alpha_4 \vec{P}_2 - \vec{k}'}^{(0)} \right]^{-1}, \quad (\text{B2})$$

with the unscreened Coulomb potential $V_{\vec{k}} = -e^2/\epsilon_0 k^2 \Omega_0$. Due to the ion's heavy mass, we neglect the transfer momentum \vec{k} in the intermediate propagator as well as the kinetic energy $\hbar^2 P^2/2M$. Replacing the Matsubara frequencies Ω_λ and Ω_κ by their on-shell values, we can perform the summations over momenta in Eq. (4) and arrive at the familiar expression Eq. (7).

APPENDIX C: CALCULATION OF THE INTERACTION STRENGTH

The expression Eq. (8) has to be evaluated. We rewrite it as

$$V_{\alpha_1, \alpha_2}^{\text{vdW}}(R) = -\frac{C_6(\alpha_1, \alpha_2)}{R^6} \\ = -\frac{e^4}{(4\pi\epsilon_0)^2 R^6} \sum' \frac{|\langle \alpha_1 \alpha_2 | W | \alpha_3 \alpha_4 \rangle|^2}{E_{\alpha_1}^{(0)} + E_{\alpha_2}^{(0)} - E_{\alpha_3}^{(0)} - E_{\alpha_4}^{(0)}}. \quad (\text{C1})$$

The primed sum indicates summation only over states, which assure a finite denominator.

Henceforth, we assume one atom in a low-lying excited state $\alpha_1 = n_1 l_1$, $n_1 = 2, 3, 4, 5$, and the second atom in its ground state, $\alpha_2 \equiv 0$. Then, virtual excitations to highly excited states α are more probable than those to states with energy smaller than $E_{\alpha_1}^{(0)}$. We can neglect the energies of those virtually excited states E_{α_3} and E_{α_4} against the sum of energy of the ground state energy and of the lowly excited state $E_0^{(0)} + E_{\alpha_1}^{(0)} = -\text{Ry}(1 + 1/n_1^2)$. Eq. (C1) becomes

$$C_6(\alpha_1, 0) = \left(\frac{e^2}{4\pi\epsilon_0} \right)^2 \frac{1}{(1 + 1/n_1^2) \text{Ry}} \sum'_{\alpha_3 \alpha_4} |\langle \alpha_1 0 | W | \alpha_3 \alpha_4 \rangle|^2 \quad (\text{C2})$$

$$= \left(\frac{e^2}{4\pi\epsilon_0} \right)^2 \frac{1}{(1 + 1/n_1^2) \text{Ry}} \sum_{\alpha_3 \alpha_4} \langle \alpha_1 0 | W | \alpha_3 \alpha_4 \rangle \langle \alpha_3 \alpha_4 | W | \alpha_1 0 \rangle - |\langle \alpha_1 0 | W | \alpha_1 0 \rangle|^2 \quad (\text{C3})$$

$$= \left(\frac{e^2}{4\pi\epsilon_0} \right)^2 \frac{1}{(1 + 1/n_1^2) \text{Ry}} \langle \alpha_1 0 | W^2 | \alpha_1 0 \rangle. \quad (\text{C4})$$

The diagonal matrix element of W vanishes for atoms with no permanent electric dipole moment. Choosing the nucleus-nucleus axis parallel to the x -axis of the coordinate system, the operator W reads

$$W = y_1 y_2 + z_1 z_2 - 2x_1 x_2. \quad (\text{C5})$$

Since the expectation values of any coordinate x, y or z vanishes, e.g. $\langle \alpha_1 0 | r_i | \alpha_1 0 \rangle = 0$, $i = 1, 2, 3$, the mixed terms in W^2 vanish. We obtain

$$C_6(\alpha_1, 0) = \left(\frac{e^2}{4\pi\epsilon_0} \right)^2 \frac{1}{(1 + 1/n_1^2) \text{Ry}} \langle \alpha_1 0 | y_1^2 y_2^2 + z_1^2 z_2^2 + 4x_1^2 x_2^2 | \alpha_1 0 \rangle \quad (\text{C6})$$

$$= \left(\frac{e^2}{4\pi\epsilon_0} \right)^2 \frac{1}{(1 + 1/n_1^2) \text{Ry}} \left[\right. \quad (\text{C7})$$

$$\left. \langle 0 | y_1^2 | 0 \rangle \langle \alpha_1 | y_2^2 | \alpha_1 \rangle + \langle 0 | z_1^2 | 0 \rangle \langle \alpha_1 | z_2^2 | \alpha_1 \rangle + 4 \langle 0 | x_1^2 | 0 \rangle \langle \alpha_1 | x_2^2 | \alpha_1 \rangle \right], \quad (\text{C8})$$

and with

$$\langle r_i^2 \rangle = \frac{1}{3} \langle r^2 \rangle \quad (\text{C9})$$

$$C_6(\alpha_1, 0) = \left(\frac{e^2}{4\pi\epsilon_0} \right)^2 \frac{1}{(1 + 1/n_1^2) \text{Ry}} \frac{2}{3} \langle 0 | r^2 | 0 \rangle \langle \alpha_1 | r^2 | \alpha_1 \rangle . \quad (\text{C10})$$

Using

$$\langle nl | r^2 | nl \rangle = \frac{n^2 a_B^2}{2} [5n^2 + 1 - 3l(l+1)] , \quad (\text{C11})$$

we finally obtain Eq. (10).

Note, that for the case, that the first atom is also in its ground state, i.e. $\alpha \equiv 0$, $C_6(00) = 12$ is obtained. The difference to the London-Eisenschitz result 12.94 is due to the neglectance of virtual bound-free and free-free transitions in the calculation presented above. For excited states, which are considered in this work, this contribution becomes negligible.

APPENDIX D: EVALUATION OF THE VAN DER WAALS PROFILE

We start with the general form of expression (7), i.e. the intensity distribution of a given spectral line, due to interaction between the radiator, which is in state $|i\rangle$ before the transition and in state $|f\rangle$ after the transition and the perturber $i, i = 1 \dots N$ in state $|n_i\rangle$. It is obtained by performing an averaging procedure over the distribution of the N perturbing atoms,

$$I_{if}(\Delta\omega) = \int d^3\vec{r}_1 \int d^3\vec{r}_2 \dots \int d\vec{r}_N P_N(\vec{r}_1, \vec{r}_2, \dots, \vec{r}_N) \delta \left(\sum_{j=1}^N V_{i\alpha_j}(r_j) - V_{f\alpha_j}(r_j) - \Delta\omega \right) . \quad (\text{D1})$$

Here, $P_N(\vec{r}_1, \dots, \vec{r}_N)$ is the probability density for having atom 1 in the volume element $d^3\vec{r}_1$ at \vec{r}_1 , atom 2 in the volume element $d^3\vec{r}_2$ at \vec{r}_2 , and so forth. It can be expanded in a cluster decomposition as

$$P_N(\vec{r}_1, \vec{r}_2, \dots, \vec{r}_N) = \frac{1}{V^N} \left(1 + \sum_{j < k} g_2(\vec{r}_j, \vec{r}_k) + \sum_{j < k < l} g_3(\vec{r}_j, \vec{r}_k, \vec{r}_l) + \dots \right) , \quad (\text{D2})$$

where the lowest non-ideal term is the pair distribution function, giving the probability to find a second particle at \vec{r}_k if there is one particle at \vec{r}_j .

The N^3 -fold integral in Eq. (D1) can be evaluated using the Fourier representation of the delta function,

$$\delta(\Phi - \Delta\omega) = \frac{1}{2\pi} \int_{-\infty}^{\infty} d\rho e^{i\rho(\Phi - \Delta\omega)} , \quad (\text{D3})$$

with $\Phi = \sum_{j=1}^N [V_{i\alpha_j}(r_j) - V_{f\alpha_j}(r_j)]$. In the case of statistically independant atoms, which are all in the same quantum state $\alpha_j \equiv \alpha_p$ i.e. $P_N(\vec{r}_1, \vec{r}_2, \dots, \vec{r}_N) = V^{-N}$, one immediatly finds

$$I_{if}(\Delta\omega) = \frac{1}{2\pi} \left(\frac{4\pi}{V} \right)^N \int_{-\infty}^{\infty} d\rho e^{-i\Delta\omega\rho} \left[\int d\vec{r} r^2 e^{i\rho[V_{i,\alpha_p}(r) - V_{f,\alpha_p}(r)]} \right]^N . \quad (\text{D4})$$

Using the van der Waals limit of the atom-atom potential, Eq. (9), Eq. (D4) turns to

$$I_{if}^{\text{vdW}}(\Delta\omega) = \frac{1}{2\pi} \left(\frac{4\pi}{V} \right)^N \int_{-\infty}^{\infty} d\rho e^{-i\Delta\omega\rho} \left[\int d\vec{r} r^2 e^{-i\rho C_6/r^6} \right]^N . \quad (\text{D5})$$

Eq. (D5) can be evaluated in the thermodynamic limit, i.e. $V \rightarrow \infty, N \rightarrow \infty$, while keeping constant the density of neutrals $N/V = n_{\text{atom}} = \text{const}$, as shown by Margenau [22]. The result is given in Eq. (14).